# Validation of a camera-based intra-hour irradiance nowcasting model using synthetic cloud data

Philipp Gregor[1], Tobias Zinner[1], Fabian Jakub[1], and Bernhard Mayer[1]

[1]Ludwig-Maximilians-Universität München, Munich, Germany

**Correspondence:** P. Gregor (philipp.gregor@lmu.de)

**Abstract.** This work introduces the novel short-term nowcasting model MACIN, which predicts direct normal irradiance (DNI) for solar energy applications based on hemispheric sky images from two all-sky imagers (ASI). With a synthetic setup based on simulated cloud scenes, the model and its components were validated in depth. We trained a convolutional neural network on real ASI images to identify clouds. Cloudmasks are generated for the synthetic ASI images with this network. Cloud height and motion are derived using sparse matching. In contrast to other studies, all derived cloud information from both ASIs and multiple timesteps are combined into an optimal model state using techniques from data assimilation. This state is advected to predict future cloud positions and compute DNI for lead times up to $20$ minutes. For the cloudmasks derived from the ASI images we found a pixel accuracy of $94.66\%$ compared to the references available in the synthetic setup. The relative error of derived cloud base heights is $4\%$ and cloud motion error is in the range of $0.1\mathrm{ms}^{-1}$. For the DNI nowcasts, we found an improvement over persistence for lead times larger than one minute. Using the synthetic setup, we computed a DNI reference for a point and also an area of $500\mathrm{m} \times 500\mathrm{m}$. Errors for area nowcasts as required, e.g., for photovoltaics plants, are smaller compared to errors for point nowcasts. Overall, the novel ASI nowcasting model and its components proved to work within the synthetic setup.

## 1 Introduction

Clouds are a major modulator of atmospheric radiative transfer, as showcased by their ability to shadow the ground. This influence on the irradiance impacts the production of renewable energy through photovoltaic (PV) and concentrating solar power (CSP) plants. These fluctuations in produced power are a limitation for the usability of PV power. Unexpected variations in power production pose a challenge for the integration into power grids (Katiraei and Agüero, 2011). Prior knowledge of upcoming fluctuations and therefore short-term irradiance prediction can help mitigate this drawback of PV power production (e.g., West et al., 2014; Boudreault et al., 2018; Law et al., 2016; Chen et al., 2022; Samu et al., 2021; Saleh et al., 2018).

Since direct irradiance can be blocked completely by clouds within seconds to minutes, knowledge of future direct irradiance is especially important for solar energy applications. Diffuse irradiance depends on complex 3D radiative transfer through the atmosphere. Variations in irradiance on the ground are relevant for solar energy applications mainly due to variations in direct irradiance (Chow et al., 2011). This study is therefore focused on direct irradiance. Nowcasting of diffuse and global irradiance is not addressed. Multiple models for intra-hour direct normal irradiance (DNI) nowcasting have been developed to predict

the variability of direct irradiance. Many of these rely on so called all-sky imagers (ASI), ground based cameras that capture hemispheric sky images (e.g., Chow et al., 2011; Peng et al., 2015; Schmidt et al., 2016; Kazantzidis et al., 2017; Nouri et al., 2022). The general idea is to extract cloud information from these images, predict future cloud positions and accordingly estimate irradiance for the next minutes. The applicability of low cost consumer grade cameras makes setups with multiple ASIs financially feasible, and increasing sizes of installed PV plants also require more measurement positions to expand nowcast areas. The Eye2Sky (Blum et al., 2021) network showcases the widespread use of multiple ASIs for regional coverage and nowcasting.

Common tasks for ASI based DNI nowcasting are the extraction of cloud position and motion. Li et al. (2011) established a method to classify pixels based on color values and thresholding. A library of reference clearsky images was introduced to extend this method and consider different atmospheric conditions and background variations for the large field of view of ASIs (Shields et al., 2009; Chow et al., 2011; Schmidt et al., 2016). Also convolutional neural networks (CNN) have been proven to work beneficially for these tasks (Ye et al., 2017; Dev et al., 2019; Xie et al., 2020; Hasenbalg et al., 2020) when trained on densely labeled data. Fabel et al. (2022) demonstrated the use of a CNN to distinguish not only clear and cloudy pixels, but further separated clouds into three subclasses for low, mid, and high layer clouds. Further on, Blum et al. (2022) projected cloudmasks of multiple imagers onto a common plane and combined them for an analysis of spatial variations of irradiances. Masuda et al. (2019) combined a camera model with synthetic images of LES cloud fields to derive fields of cloud optical depth from images instead of simple cloudmasks.

Setups with multiple ASIs allow for the estimation of cloud base height using stereography (Nguyen and Kleissl, 2014; Beekmans et al., 2016; Kuhn et al., 2018b). Nouri et al. (2018) used four ASIs to derive height information and even a 3-dimensional cloud representation for irradiance nowcasting. Three ASIs were used by Rodríguez-Benítez et al. (2021) for three independent DNI nowcasts, which are finally averaged into a mean DNI nowcast.

Whilst measurements of irradiance through pyranometers are point measurements, nowcasting methods are usually targeted at solar power plants and therefore receiver areas. Kuhn et al. (2017a) derived area irradiance values using a camera monitoring shadows on the ground in combination with point irradiance measurements. ASI nowcasts for areas were found to outperform persistence for situations with high irradiance variability (Kuhn et al., 2017b). Nouri et al. (2022) computed ASI nowcasts for eight pyranometer measurement sites distributed over roughly $1\mathrm{km}^2$. This study found reduced errors if nowcasts and measurements were averaged over all sites before error calculation in comparison to errors of individual point nowcasts.

Apart from application on real world images, Kurtz et al. (2017) applied a DNI nowcasting model to synthetic ASI images of cloud scenes from large eddy simulation (LES) models. The images were generated using a 3D radiative transfer model. This synthetic application comes with the advantage of optimal knowledge of the atmospheric state and allows for extended evaluation. The study showcased the problems introduced by the viewing geometry of ASIs.

In this study, we introduce a novel model for all-sky image based cloud and direct irradiance nowcasting (MACIN) and use synthetic data to validate it. This DNI nowcasting model is based on a setup with two ASIs. We use state of the art techniques, e.g., to derive cloudmasks using a CNN that was trained on sparsely labeled data. Cloud base height (CBH) is derived by stereography and cloud motion by sparse matching. The derived cloud information is fed into a horizontal model grid using

a method inspired by data assimilation. The method has similarities to the cloudmask combination of Blum et al. (2022) but allows the use of images from multiple timesteps and is used for nowcasting future states and not just analyzing the current situation. Predicted cloudiness states are projected to the ground and converted into DNI. We apply the techniques to synthetic ASI images generated from simulated LES cloud fields. This allows us to validate the derived quantities as well as the overall nowcast performance. Further on, this allows for in depth validation of DNI nowcasts not just for single point measurements but also for areas, which is important for PV and CSP plants. Sect. 2 describes the synthetic data used throughout the study, the methods to derive information from ASI images as well as the MACIN nowcasting model. The quantities and metrics used for validation are explained in this section as well. Sect. 3 describes the validation of derived cloudmasks, cloud base height, cloud motion, and the full DNI nowcasting model. Results of the validation are analyzed and discussed to affirm the presented methods and explain error sources. Conclusions can be found in Sect. 4 as well as a brief description of possible follow-up work.

## 2 Methods

The methods and data are described in this section. This includes an explanation of the synthetic data and all-sky images as well as the methods used to derive information about clouds in Sect. 2.1. The DNI nowcasting model that utilizes this information is outlined in Sect. 2.2. Reference quantities and metrics for validation are given in Sect. 2.3.

### 2.1 Synthetic data and all-sky images

The synthetic data has been prepared by Jakub and Gregor (2022). This dataset is a $6\mathrm{h}$ LES run computed with the cloud model UCLA-LES (Stevens et al., 2005). Horizontal resolution is $25\mathrm{m}$ and LES output fields are given every $10\mathrm{s}$. The initial atmospheric profile was chosen to produce a single shallow convection cloud layer with cloud base height of roughly $1000\mathrm{m}$ developing from cloud fraction of $0\%$ in the beginning to roughly $100\%$ at the end of the simulation after $6\mathrm{h}$. The reader is referred to Jakub and Gregor (2022) for more details and impressions of the cloud scenes used in this study.

This dataset provides realistic cloud situations and allows for detailed benchmarking. Cloud liquid water content ($lwc$) is the most important variable of the dataset for this study. To calculate the optical properties of clouds, the effective radius is also needed. Since the LES output field does not contain this information, a fixed number density of $120 \cdot 10^6 \mathrm{m}^{-3}$ was assumed. The effective radius of cloud droplets was calculated following Bugliaro et al. (2011). For simplicity, other atmospheric parameters like water vapor, temperature, pressure, and molecular composition from the LES output are neglected within this study and the US Standard Atmosphere (Anderson et al., 1986) is assumed. While these atmospheric parameters and their variations are in general not negligible for radiative transfer, the setup for this study was simplified to focus on clouds as a major modulator of irradiance. Within this study, the sun was assumed to be at a constant zenith angle of $30°$ to the south.

We assume a fisheye camera model corresponding to the OpenCV fisheye module Bradski (2000) for synthetic images generated from these LES cloud fields. The parameters for this projection model were derived from the calibration of a CMS Schreder ASI-16 camera. This ASI features an $180°$ FOV fisheye objective to capture hemispheric images of the cloud situation.

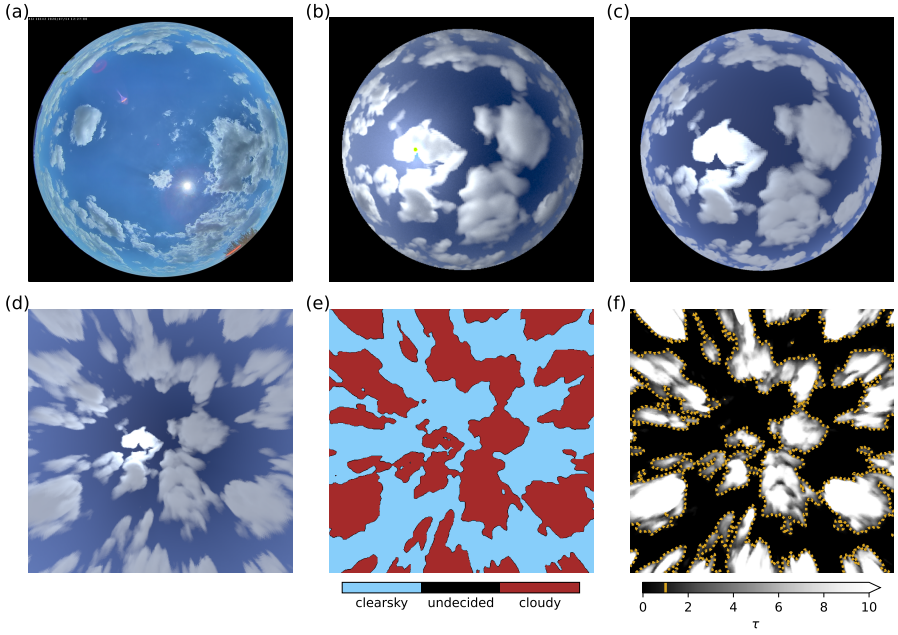


**Figure 1.** (a) Real ASI image captured with a CMS Schreder ASI-16 in the Bavarian countryside (48°10'50.3"N, 11°00'27.4"E) on 14 July 2020. (b-d) Synthetic images for LES time 9900s generated using (b) MYSTIC, (c) ray-marching and (d) ray-marching followed by projection. (e) Cloudmask derived from the projected ray-marching image and (f) LES cloud optical depth $\tau$ in the line of sight with additional yellow contour illustrating $\tau_{\mathrm{thresh}} = 1.0$. Only few pixels are labelled *undecided* by the CNN as depicted in (e).

This study employs two distinct approaches to generating all-sky images from LES cloud scenes. We generate images with the viewing geometry derived according to the fisheye camera model for the ASI-16 camera. As our methods are developed to work with cameras that are not necessarily calibrated spectrally, the images are only roughly optimized to resemble the colors of the ASI-16. We use a simple spectral camera model with whitebalance, black level, gamma correction, and an upper intensity limit to convert radiances into pixel values.

One of the image generation methods uses synthetic radiances from the Monte Carlo 3D radiative transfer model MYSTIC (Mayer, 2009), which does not introduce any simplifying assumptions in radiative transfer. These radiances can be converted into synthetic images using the camera model. While MYSTIC radiances are physically correct, they are computationally expensive. Computation of these radiances for a single image requires multiple CPU hours and therefore this approach was used for 29 images with a resolution of $240 \times 240$ pixel only. In contrast, our second approach is only a rough approximation of radiative transfer. We use a ray-marching technology commonly applied in the computer gaming industry (e.g.; Schneider, 2018; Hillaire, 2016) to trace through volumetric media. Many small steps along the line of sight are marched through the atmosphere for every pixel. At every step, in-scattered light into the line of sight of the simulated imager is computed using local optical properties of the atmosphere. This is summed up to compute the overall light reaching the simulated imager. Schneider (2018) computes the direct radiation from the sun at each step to estimate the amount of light scattered into the

line of sight of the imager. Multiple scattering is only roughly parametrized in this approach, although it may be dominant in regions of high cloud optical thickness. We therefore use the original marching together with a different method to calculate the amount of in-scattered light. Direct and diffuse irradiances are calculated with a two-stream radiative transfer model (Kylling et al., 1995) on tilted independent columns of the LES cloud field. For each ray-marching step, local irradiances are used to estimate the amount of direct and diffuse light scattered towards the simulated imager. This technique is implemented using the OpenGL framework and allows us to generate images of $960 \times 960$ pixel within seconds. Generated images are interpolated to the original ASI resolution in a postprocessing step for both generation methods. Figures 1a-c show a real world image as well as images generated using MYSTIC and ray-marching. Because of the low computational cost of image generation, we work with ray-marching images throughout this work if not stated otherwise. We derived cloudmasks from both MYSTIC and ray-marching images to confirm the usability of the latter for our purpose.

As a first step in working with generated images, the camera model is applied to project them onto a horizontal, ground parallel image plane. During reprojection, image features may be distorted and blurred. But reprojection allows to work on an image plane parallel to the ground simplifying further image processing. Figures 1c and 1d display an image as captured by the ASI and its projected correspondence as generated using ray-marching. While the original ASI resolution is $1920 \times 1920$ pixel, we project images to $480 \times 480$ pixel for use within our nowcasting model.

#### 2.1.1 Cloudmasks

The most important information to obtain from all-sky images is the classification of pixels as cloudy or clear. Convolutional neural networks (CNN), which are commonly applied for image segmentation, have also been applied to images of clouds to generate cloudmasks (e.g., Dev et al., 2019; Xie et al., 2020; Fabel et al., 2022). Our cloudmask derivation relies on CNN as well. We used the DeeplabV3+ network structure (Chen et al., 2018). The setup and training of the CNN are outlined briefly in the following, a more detailed explanation can be found in Appendix A1 as well as a description of the hand labeling process of training data. Real world images from an ASI-16 were chosen for this training dataset to avoid overfitting to generated ASI images of the limited LES dataset and allow for easy future application of MACIN to real world setups. Note that this is the only real measurement used throughout this study, measurements otherwise refer to generated ASI images and simulated DNI. Training was done using 793 hand labeled projected images depicting various cloud situations. Segmentation classes are *cloudy*, *clear*, and *undecided*. As the definition of *cloudy* and *clear* areas in images is often hard even for human observers, the CNN training is designed to ignore *undecided* image regions. The CNN is set up to reproduce the *cloudy* and *clear* labeled regions, but is free to fill in regions labeled as *undecided* by hand without impacting the training. The CNN thus fills in regions for which the cloud state is ambiguous or indistinctable to humans based on the definition of *cloudy* and *clear* for regions, where this is obvious for humans. From the CNN, we obtain cloudmasks as a segmentation of an ASI image into the classes *cloudy*, *undecided*, and *clear* with respective scalar values of $1.0$, $0.5$, and $0.0$. Figures 1d and 1e give a synthetic image and the derived cloudmask. For comparison, the LES cloud optical depth ($\tau$) traced in the line of sight for each pixel is given in Fig. 1f.

### 2.1.2 Cloud base height from stereo matching

In order to map cloudmasks to 3-dimensional coordinates, cloud base height (CBH) is required. For the experiments presented here, two ASIs are located in a $500\mathrm{m}$ north-south distance. I.e., for each timestep two viewing angles can be exploited to derive CBH. Features from simultaneous ASI images of the same cloud scene are sparsely matched using efficient coarse to fine patchmatch (CPM; Hu et al., 2016), a pixel based pyramidal matching method. For a grid of pixels on the first input images, DAISY feature descriptors (Tola et al., 2010) are computed and their best matching counterparts in the second image are determined. As a result, we obtain a list of matched pixels from both images, which are supposed to depict the same part of a cloud. We use the derived cloudmasks to filter matched pixels, these must be marked as *cloudy* in the corresponding cloudmasks for both images to be accepted. Using the known camera geometry, a cloud base height can be derived for each matched pair of pixels with the mis-pointing method developed by Kölling et al. (2019). This results in up to multiple thousand feature positions per pair of simultaneously captured images which theoretically allows for a fine grained treatment of CBH. However, the nowcasting model presented in this study currently assumes a single cloud layer. Therefore an image wide average CBH is derived from the mean height of the feature positions.

### 2.1.3 Cloud motion

Cloud motion needs to be derived to predict future shading by clouds. Using the CPM matching algorithm on consecutive images taken in intervals of $60\mathrm{s}$, we obtain matches describing the displacement of features. Computed cloudmasks are used again to exclude matches lying outside of detected cloud areas. Average image cloud base height and camera model are used to scale detected pixel movement to physical velocities within the assumed plane of clouds. A dense cloud motion field is obtained by nearest neighbor interpolation of these sparse velocities.

## 2.2 Nowcasting model

The nowcasting model presented in the following uses derived cloudmasks, CBH and cloud motion to predict future cloud situations and corresponding irradiance estimates. Cloudmasks and cloud motion are represented as variables on a horizontal 2-dimensional grid, which will be referred to as cloudiness state and velocities. The 2-dimensional grid and all input data are assumed to be on one horizontal, ground parallel level at the height given by the derived CBH. Multi-level clouds are not yet represented as such by our model. Future states of these 2-dimensional fields are predicted using a simple advection scheme. Irradiance estimates are computed from these future cloudiness states. All derived cloudmasks and cloud motions are combined into an optimized initial state of the horizontal 2-dimensional fields. The nowcasting model therefore consists of three major parts: a simple advection method, a method inspired by data assimilation to determine the initial state, and a radiative transfer parametrization to calculate DNI from the cloudiness state. These three parts are explained more closely in the following.

### 2.2.1 Advection scheme

The nowcasting model is based on a 2-dimensional grid with grid spacing of $\Delta x = \Delta y = 10\mathrm{m}$ and number of grid points $N = M = 1600$ in $x$- and $y$-direction respectively, therefore covering $16\mathrm{km} \times 16\mathrm{km}$. Variables on each grid point are cloudiness state $\mathrm{cm}$ and cloud velocities $u$ and $v$ in $x$- and $y$-direction respectively. Starting from an initial state at the first iteration $t_0 = 0\mathrm{s}$ and a temporal resolution of $\Delta t = 60\mathrm{s}$, future cloudiness states at times $t_i = t_0 + i \cdot \Delta t$ are computed using advection as

$$\mathrm{cm}_{t_{i+1}}(n,m) = \mathrm{cm}_{t_i}(\tilde{n},\tilde{m}), \tag{1}$$

$$\tilde{n} = n - int(\lambda \cdot u(n,m)), \tag{2}$$

$$\tilde{m} = m - int(\lambda \cdot v(n,m)), \tag{3}$$

where $\lambda = \Delta t / \Delta x$. The coordinates $(\tilde{n},\tilde{m})$ determined by advection using physical velocities are restricted to discrete grid coordinates and therefore integers. This constrains actually representable velocities to multiples of $\Delta x / \Delta t$. Continuous boundary conditions are assumed. The same advection scheme is applied to the horizontal velocities fields $u_t(n,m)$ and $v_t(n,m)$ as well.

### 2.2.2 Data Assimilation

Cloudmask and horizontal velocity field from one imager and timestep together with an estimation of cloud base height would be sufficient to initialize the advection model. However, for each nowcast we do have cloudmasks and velocities from two imagers with different viewing geometries and multiple timesteps. In order to make use of as much information as possible for the initial state, we employ a method similar to 4D-var data assimilation (Le Dimet and Talagrand, 1986) in numerical weather prediction models. The general idea is to define a scalar function of an initial model state that measures differences of model states and measurements. This so called cost function is then iteratively minimized to find an optimal model state for given measurements and cost function. We reference "measurements" in this section and the following. We thereby mean the synthetic generated ASI images and simulated DNI values and not real measurements.

The difference of model state and measurements needs to be assessed at matching times. Model states for multiple time steps are therefore computed from the initial state at time $t_0$ using the previously described advection $M$. Model cloudiness states at time $t_k$ will be denoted as $\mathrm{cm}(t_k) = M(\mathrm{cm}, t_k)$ with initial cloudiness state $\mathrm{cm}$. Horizontal velocities $u$ and $v$ are described analogously. We define the cost function $J$ for $L$ timesteps in the interval $[t_0, t_l]$ and two ASIs ($p \in 1,2$) as

$$\begin{aligned} J(\mathrm{cm},u,v) = \sum_{N,M} \sum_{l=0}^{L} \sum_{p=1}^{2} \quad & \left( \frac{1}{\sigma_{\mathrm{cm}}} \cdot \left(\mathrm{cm}(t_l) - \mathrm{cm}_{\mathrm{meas},l,p}\right)^2 \right. \\ & + \frac{1}{\sigma_{uv}} \cdot \left(u(t_l) - u_{\mathrm{meas},l,p}\right)^2 \\ & \left. + \frac{1}{\sigma_{uv}} \cdot \left(v(t_l) - v_{\mathrm{meas},l,p}\right)^2 \right) \\ & + R(u,v) \end{aligned} \tag{4}$$

with measurements of cloudmasks $\mathrm{cm}_{\mathrm{meas},l,p}$ and horizontal velocities at timestep $l$ from imager $p$ interpolated to the model grid. Summation over all grid points is indicated by $\sum_{N,M}$ for better readability. The coefficients $\sigma_{\mathrm{cm}} = 0.1$ and $\sigma_{uv} = 10.0\mathrm{ms}^{-1}$ are supposed to account for uncertainties in the respective measurements but are mainly used as tuning parameters here. More complex, non-scalar coefficients could differentiate e.g. for varying measurement quality within ASI images or between different imagers but require characterization of the system, which is usually not available. The additional regularization term denoted as $R(u, v)$ is used to suppress measurement errors, especially outliers in the velocity field. In detail, it is

$$R_{uv}(u, v) = \sigma_{R,uv} \cdot \left( (\nabla u)^2 + (\nabla v)^2 \right) \tag{5}$$

with tuning parameter $\sigma_{R,uv} = 250\mathrm{s}^{-1}$ chosen to smooth the velocity field. As cloudmasks are especially hard to derive from ASI images in the bright region of the sun, measurement values are excluded from assimilation if they are derived from an image region of $2.5°$ around the sun. Erroneous cloudmask values derived for the bright sun and zero velocities derived from the static sun position are thereby avoided. Fig. 2 illustrates the measurements, first guess, and analysis state after assimilation for an example assimilation run. Due to the limited complexity of the advection scheme and the high resolution observations from images, a background state is not used. Model states of previous nowcast runs are not used within assimilation. This means successive nowcast runs are independent, as states from previous model runs for the nowcast start time are not considered in additional terms in Equ. 4. Average cloudiness state and velocities from all measurements available at the time of the initial state are used as a first guess for cost function minimization. The cost function is minimized using the bounded L-BFGS-B algorithm (Zhu et al., 1997). For efficient optimization, the advection model and cost function were implemented using the PyTorch framework (Paszke et al., 2019), which allows for automatic calculation of the adjoint of the cost function. The optimized model state is finally used for the actual nowcast as the initial state of the advection model.

### 2.2.3 Radiative transfer parametrization

Direct solar irradiance is reduced by interaction with molecules, aerosol and clouds. For this study, we assume that short term changes in direct irradiance are mainly caused by clouds and neglect other variations. DNI is parametrized using previous irradiance measurements on site together with predicted cloudmasks. "Measurements" in the following do not describe real world measurements with, e.g., a pyranometer, but instead DNI values simulated for LES scenes. The idea of the parametrization is to derive references for occluded and non-occluded cases from measurements. Depending on the cloudiness state, DNI is then interpolated from these references. Therefore, a time series of clearsky index values (CSI) $k$ is constructed from DNI measurements as the ratio of measurements and a simulated clearsky $\mathrm{DNI}_{\mathrm{clear}}$. From this time series, values for $k$ are extracted for two sub-series: occluded ($k > 0.9$) and non-occluded ($k < 0.1$) times. We define the occluded CSI $k_{\mathrm{occl}}$ and non-occluded CSI $k_{\mathrm{clear}}$ as the exponentially weighted mean with a half life time of $10\mathrm{min}$ from respective measurement subsets. CSI values for a non occluded and a fully occluded sun are interpolated linearly. A sun disk of $0.5°$ opening angle at the given sun elevation and azimuth is projected onto the 2-dimensional model grid. The mean cloudiness state of all grid points in the sun disk ($\mathrm{cm}_{\mathrm{sun}}$) is used to calculate DNI for time $t$ as

$$\mathrm{DNI}(t) = \mathrm{DNI}_{\mathrm{clear}} \cdot ((1 - \mathrm{cm}_{\mathrm{sun}}(t)) \cdot k_{\mathrm{clear}} + \mathrm{cm}_{\mathrm{sun}}(t) \cdot k_{\mathrm{occl}}) \tag{6}$$

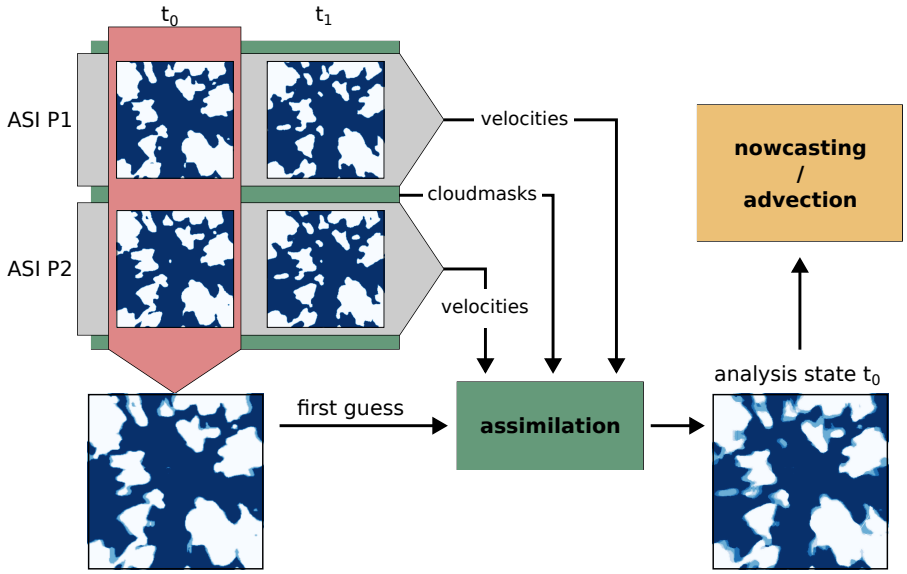


**Figure 2.** Illustration of cloudmask measurements, derived first guess used for assimilation and analysis state found by assimilation for LES time $t_0 = 8940\text{s}$. Shown is the cloudiness state and the inner $8\text{km} \times 8\text{km}$ of the domain. The analysis state is less sharp on cloud edges due to consideration of multiple cloudmask measurements.

The exponentially weighted mean is used for the computation of $k_{\text{occl}}$ and $k_{\text{clear}}$ in order to smooth latest fluctuations and provide a values for all times.

### 2.3 Synthetic data experiment setup

The synthetic setup allows us to compare quantities derived by the nowcasting model to synthetic reference values. Within this study we simulate a setup around a fictional $500\text{m} \times 500\text{m}$ area PV power plant. As depicted in Fig. 3, all-sky images are generated for synthetic imagers at positions P1 and P2 centered on the northern and southern boundaries of this area. Direct normal irradiance values were calculated for point P1 and the full $500\text{m} \times 500\text{m}$ area A1 as explained later on. Images are rendered with MYSTIC and ray-marching as explained in Sect. 2.1 for a synthetic ASI at P0 at the south-eastern edge of A1 to compare both methods. Ray-marching images for P1 and P2 are used for actual nowcasting and all other applications in this study.

Validation quantities used within the experiments in Sect. 3 are explained in the following. Cloud optical depth ($\tau$) is traced in the line of sight for every pixel of the corresponding ASI image and used to validate derived cloudmasks. By applying a threshold to the resulting $\tau$-fields we can calculate reference cloudmasks. Fig. 1f shows an example $\tau$-field. These are used for the validation of the derived CNN cloudmasks. Cloud base height reference is computed in compliance with the view of an ASI. The last scattering of light before reaching the ASI sensor gives the origin of pixel information, in this case cloud height as seen from below. MYSTIC can be used not only to compute radiances, but also to obtain these scattering positions. A cloud

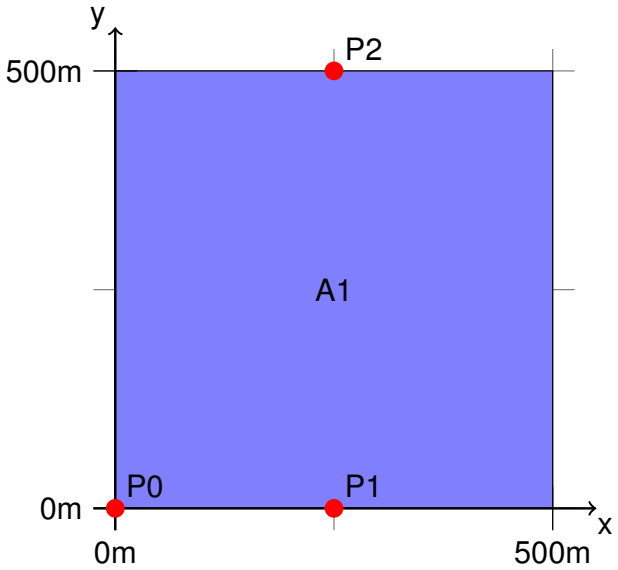


**Figure 3.** Spatial setup for the synthetic experiments conducted in this study. Shown are the ground coordinates within the LES domain. Synthetic all-sky images were generated at points P0, P1 and P2. Direct normal irradiance was simulated for point P1 and area A1. Nowcasts rely on images from P1 and P2 and predict values for point P1 and area A1.

motion reference is hard to define as clouds in the LES simulation – as in nature – are not moving as solid objects but may change size and shape or even appear and disappear. Wind velocities at cloud level may therefore not be an exact benchmark for the overall observable cloud motion. Within this study we use vertically integrated liquid water path ($\mathrm{lwp}$) from the LES fields as an indicator for horizontal cloud distribution. The maximum cross-correlation between domain wide $\mathrm{lwp}$ of two successive timesteps is assumed to be a reference for average cloud motion. This reference describes the mean displacement for all timesteps of the LES cloud data. However, clouds are convectively reshaping, growing, and shrinking in this data, which makes this cloud motion definition vague. The synthetic data allows for a more direct validation of cloud motion. LES cloud fields can be frozen for a timestep and their position shifted. This basically simulates scenes of pure advection without any convective effects. To simulate this advective case for cloud motion validation, we use two images of the same cloud scene but taken from different positions. The choice of an assumed time difference between the images $\Delta t$ defines the advective cloud velocity. For simplicity, we use images taken in $500\mathrm{m}$ north-south distance as represented by P1 and P2. Assuming $\Delta t = 60\mathrm{s}$ we obtain theoretical cloud velocities of $-8.3\mathrm{ms}^{-1}$ meridionally and $0\mathrm{ms}^{-1}$ zonally.

The Monte Carlo 3D RTE solver MYSTIC was used to compute radiances for images and true direct normal irradiances at ground level. We calculated direct normal irradiance for two different synthetic references, as depicted in Fig. 3. A DNI point reference is simulated at P1, and an area reference of the $500\mathrm{m} \times 500\mathrm{m}$ region A1 with ASIs centered at the northern and southern boundary at P1 and P2. As a benchmark for the DNI nowcasting model, persistence nowcasts for start time $t_0$ and

nowcast time $t$ are calculated from simulated DNI "measurements" at $\mathrm{DNI}_{\mathrm{P1}}$ as

$$\mathrm{DNI}_{\mathrm{pers}}(t) = \mathrm{DNI}_{\mathrm{meas}}(t_0). \tag{7}$$

The metrics used for validation are

$$\mathrm{RMSE} = \sqrt{\frac{1}{N}\sum_{i=1}^{N}(x_i - x_{\mathrm{ref},i})^2}, \tag{8}$$

$$\mathrm{NRMSE} = \sqrt{\frac{1}{N}\sum_{i=1}^{N}\left(\frac{x_i - x_{\mathrm{ref},i}}{x_{\mathrm{ref},i}}\right)^2} \tag{9}$$

and

$$\mathrm{MBE} = \frac{1}{N}\sum_{i=1}^{N}(x_i - x_{\mathrm{ref},i}) \tag{10}$$

with the quantity to be evaluated $x$, its corresponding reference $x_{\mathrm{ref}}$ and the number of values $N$. Additionally, we use the pixel accuracy

$$\mathrm{PA} = \frac{\mathrm{CCLD} + \mathrm{CCLR}}{N_{px}} \tag{11}$$

with the number of correctly *cloudy* or *clear* classified pixels CCLD and CCLR respectively as well as the overall number of pixels $N_{px}$.

## 3 Validation using synthetic data

### 3.1 Cloudmasks

The CNN cloudmask model was successfully trained and validated on hand labeled real world images, as explained in Appendix A1. We evaluate derived cloudmasks to show that it is reasonable to apply the cloudmask CNN to the synthetic images in this study. We calculated path cloud optical depth ($\tau$) for all viewing angles of our ASI and every desired timestep. Together with a threshold this gives a reference cloudmask. To validate pixelwise cloud classifications, we use a threshold of $\tau_{\mathrm{thresh}} = 1.0$ to create reference cloudmasks from $\tau$. Values of $\tau \geq \tau_{\mathrm{thresh}}$ are linked to *cloudy* areas in this $\tau_{\mathrm{thresh}}$-cloudmasks. We evaluated CNN cloudmasks from ray-marching images for position P1 and 360 timesteps in 60s intervals covering all LES times. The contingency table 1 displays the distribution of classes of $\tau_{\mathrm{thresh}}$-cloudmasks against our CNN cloudmasks. In general, we find very good compliance. Each of the classes *cloudy* and *clear* makes up about $50\%$ of the compared pixels, which corresponds well to the $\tau_{\mathrm{thresh}}$-cloudmasks. Cloudmasks of our CNN exhibit a slight bias towards classifying too less pixel as *cloudy*. Pixel accuracy is $\mathrm{PA} = 94.66\%$ against the $\tau_{\mathrm{thresh}}$-cloudmasks.

**Table 1.** Contingency table for cloudmask classes from CNN and cloud optical depth $\tau$ in the line of sight thresholded by $\tau_{\mathrm{thresh}} = 1$ as reference. All values are given in $\%$.

| | | reference | | |
|---|---|---|---|---|
| | | $\tau < 1.0$ | $\tau \geq 1.0$ | $\sum$ |
| CNN | *clear* | 46.43 | 2.54 | 48.97 |
| | *undecided* | 0.22 | 0.25 | 0.47 |
| | *cloudy* | 2.33 | 48.23 | 50.56 |
| | $\sum$ | 48.98 | 51.02 | 100 |

Beyond ray-marching images, we calculated 29 MYSTIC images and computed CNN cloudmasks for these. By doing the same with corresponding ray-marching images, we could ensure that the derived cloudmasks exhibit similar performance for both image generation approaches. As MYSTIC images are physically correct, we conclude that the usage of approximated ray-marching images does not affect the validity of our results.

### 3.2 Cloud base height

We used data from for the entire LES scene and effectively 319 timesteps with clouds for the validation of derived CBH. Ray-marching images taken at P1 and P2 were used to derive CBH as in the nowcasting model. Computed scattering positions give the reference CBH. As our nowcasting model assumes a single cloud base height, we average the derived CBH per image pair. Figure 4a shows derived average CBH per image pair and corresponding reference CBH. For these averaged heights, we obtain a $\mathrm{MBE}$ for the miss-pointing method of $50.7\mathrm{m}$, $\mathrm{RMSE}$ of $56.9\mathrm{m}$ and $\mathrm{NRMSE}$ of $4.0\%$. When subtracting the found bias of $50.7\mathrm{m}$ from the derived image average cloud base heights, $\mathrm{RMSE}$ could be reduced to $25.6\mathrm{m}$ and $\mathrm{NRMSE}$ to $2.6\%$. Increasing systematic error can be observed for reference CBH up to about $1400\mathrm{m}$. A histogram of all derived pixel heights, which are the basis for the averaged CBH, and their reference is shown in Fig. 4b. Similar to the image wide average cloud base height, derived pixel heights show good agreement with reference heights and a small systematic overestimation. Reference pixel heights show a wider distribution compared to derived values, resulting in stripes visible in Fig. 4. Found height errors could result from the limited resolution of images and therefore discrete viewing directions, the projection process and the discrete stepping of the image generation ray-marching algorithm. Error sources were not investigated further, as errors are in the range or even lower than those found in other studies for their derived cloud base heights (e.g., Nguyen and Kleissl, 2014; Kuhn et al., 2019; Blum et al., 2021). Equally, no additional work was done to mitigate the observed systematic errors for use in nowcasting.

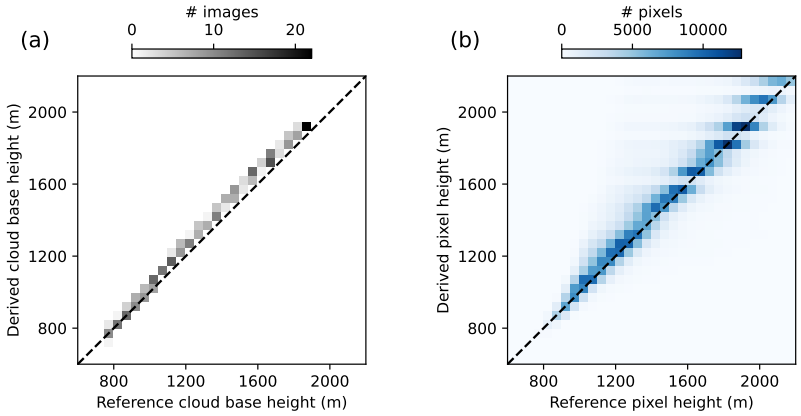


**Figure 4.** Histogram of (a) image mean cloud base height and (b) height derived for matched pixels of all images compared against synthetic references.

### 3.3 Cloud motion

As wind is not necessarily an exact benchmark for cloud motion in convective cloud scenes, we chose two ways to validate our derived cloud motion for two cases. Cloud motion according to the LES is used as a convective case where clouds also develop and decay. Additionally, we are interested in the performance when cloud motion is pure advection, i.e. only displacement of frozen cloud fields. This advective case allows to derive an exact reference for cloud motion and the convective case allows to validate the quality of the derived cloud motion in the presence of clouds that change their size and shape.

Validation of cloud motion in the convective case is done on images every $60\mathrm{s}$ for LES times from $0\mathrm{s}$ to $21540\mathrm{s}$. Figure 5 shows cloud fraction as a function of LES time. Average displacement of vertically integrated liquid water path ($\mathrm{lwp}$) between timesteps is calculated using maximum cross-correlation and used as a reference. This describes mean translation and is thereby a proxy for domain averaged reference cloud motion. Cloud motion vectors derived by sparse matching are averaged per timestep and ASI and compared against this reference. Figure 5 shows zonal and meridional winds derived for both ASI and the reference determined by $\mathrm{lwp}$ cross-correlation. The cloud fraction derived from cloudmasks of an ASI at P1 is given as an indicator of the cloud situation. Up to LES time of approximately $3600\mathrm{s}$, no significant visually detectable clouds are present and therefore no velocities derived. Up to approximately $6000\mathrm{s}$, derived velocities are relatively unstable over time, with changes in estimated velocities of up to $1.7\mathrm{ms}^{-1}$ over $60\mathrm{s}$. We relate this to the rapidly changing nature of small convective clouds in combination with a low cloud fraction. During this time, some of the small clouds appear and disappear in between timesteps and are therefore mismatched. After approximately $6000\mathrm{s}$, derived zonal velocities vary in a range of $\pm 0.5\mathrm{ms}^{-1}$ between timesteps. Zonal cloud motion close to zero matches the LES initialization without zonal wind. Meridional velocities increase from about $3\mathrm{ms}^{-1}$ at $6000\mathrm{s}$ to a maximum of $4.7\mathrm{ms}^{-1}$. In general, our derived zonal velocities show a less noisy estimate compared to the reference. Derived velocities from both ASIs show very similar patterns. This further affirms the stability of the cloud motion derivation. However, we do not have an absolute reference to benchmark derived velocities in the

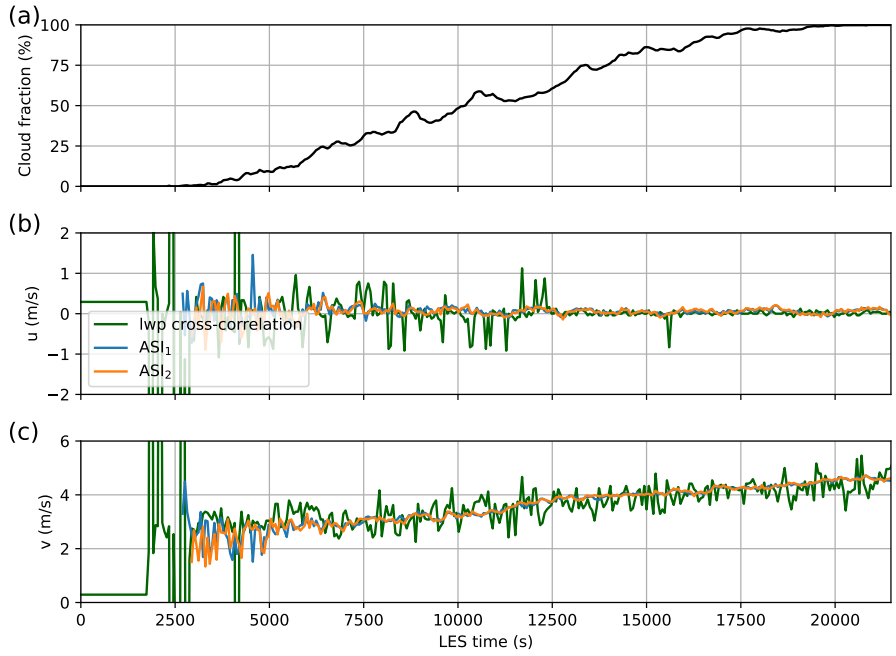


**Figure 5.** (a) Cloud fraction from cloudmasks of ASI at P1 for LES times. Per timestep scene averaged cloud motion derived using cross-correlation of the lwp-field of the LES simulation and our cloud motion derivation based on feature matching for east to west motion $u$ (b) and south to north motion $v$ (c).

convective case, as pure displacement of convective clouds is hard to capture and may differ strongly from main winds. We validate derived cloud velocities using artificially advected cloud fields to overcome this limitation. The same LES times as in the convective validation are used, but each timestep is assumed to be independent. Cloud motion is generated by freezing the cloud field and shifting it for each timestep. This results in an objective reference cloud motion. A shift of $500\mathrm{m}$ from north to south at a time difference of $60\mathrm{s}$ gives a theoretical $u$ of $0\mathrm{ms}^{-1}$ and $v$ of $-8.3\mathrm{ms}^{-1}$. No velocities were derived in the absence of clouds up to approximately $2500s$. Afterwards, the derived velocities match the theoretical displacements well with $\mathrm{RMSE}$ of $0.019\mathrm{ms}^{-1}$ zonally and $0.11\mathrm{ms}^{-1}$ meridionally.

Overall, these results prove that the derived cloud motions are reliable for the cloud situations used in this study. This can also be seen as a further validation of derived CBHs as they are necessary for the calculation of physical velocities.

### 3.4 DNI Nowcasts

Evaluation of the nowcasting model is done in multiple steps which are described and discussed in the following. MACIN is compared against persistence to evaluate overall performance. Additionally, variations of MACIN using ideal cloudmasks were run to investigate the implications of errors in CNN derived cloudmasks. These variation runs will be called *cloudmask variation* and *continuous cloudmask variation* hereafter and explained later on. Finally, a simplification of MACIN is used to

assess possible benefits of the expensive assimilation of MACIN. This variation will be referred to as *simple variation*. For MACIN and all its variations, one nowcast run was started every $60\mathrm{s}$ for LES times $60\mathrm{s}$ to $21540\mathrm{s}$ for a total of $359$ nowcast runs. Maximum nowcast lead time was chosen as $20\mathrm{min}$. Nowcast timesteps exceeding the maximum LES time of $21600\mathrm{s}$ are discarded. DNI nowcasts are always derived simultaneously for point P1 and area A1. Errors for point and area forecasts show similar characteristics. Therefore, it is discussed jointly in the following. If not stated otherwise, error values are given for point DNI and in brackets for area DNI.

Figures 6a-b show average $\mathrm{RMSE}$ and $\mathrm{MBE}$ for point nowcasts of persistence, MACIN and *cloudmask variation* grouped by lead time. Figures 6c-d give the same for area nowcasts. Errors of persistence and MACIN give the overall performance of the introduced nowcasting model and are therefore analyzed first. Persistence nowcasts start without error at lead time $0\mathrm{min}$, but $\mathrm{RMSE}$ increases strongly up to approximately constant $300\mathrm{Wm}^{-2}$ ($250\mathrm{Wm}^{-2}$) after $6\mathrm{min}$. Persistence $\mathrm{MBE}$ increases linearly up to approximately $50\mathrm{Wm}^{-2}$ linked to the tendency of growing cloud fraction over time. MACIN exhibits non-zero $\mathrm{RMSE}$ at nowcast start, but a smaller increase of $\mathrm{RMSE}$ over time compared to persistence. In terms of $\mathrm{RMSE}$, MACIN outperforms persistence for lead times larger than $1\mathrm{min}$. Improvements over persistence for these longer lead times are thereby typically on the order of $50\mathrm{Wm}^{-2}$ ($50\mathrm{Wm}^{-2}$) and more. In general, the $\mathrm{RMSE}$ of nowcasts for areas is about $50\mathrm{Wm}^{-2}$ lower compared to nowcasts for points. $\mathrm{MBE}$ is mostly negative for MACIN with magnitudes in the range of persistence $\mathrm{MBE}$. Non-zero $\mathrm{RMSE}$ at lead time $0\mathrm{min}$ may be a result of erroneous cloudmasks in the region of the sun, errors in the radiative transfer (RT) parametrization or smearing out during the assimilation because of multiple time steps and viewing geometries.

To further investigate the initial nowcast error discussed above, a *cloudmask variation* of MACIN was run. Perfect cloudmasks were used as input for the nowcasting model instead of CNN cloudmasks. These perfect cloudmasks are derived from the LES cloud optical depths in the line of sight $\tau$ (see also Sect. 3.1 and Fig. 1f) with a threshold of $\tau_{\mathrm{thresh}} = 1.0$ to distinguish between *cloudy* and *clearsky*. By using these perfect cloudmasks for nowcasting, influence of cloudmask errors within the nowcasting model can be assessed. As for the persistence and MACIN, nowcast errors for the *cloudmask variation* are given in Fig. 6. $\mathrm{RMSE}$ of the *cloudmask variation* is very similar to the $\mathrm{RMSE}$ of MACIN. This suggests that the CNN cloudmasks provide a good estimate of the cloud situation for our nowcasting. However, the *cloudmask variation* outperforms MACIN by $31\mathrm{Wm}^{-2}$ ($32\mathrm{Wm}^{-2}$) for lead time $0\mathrm{min}$ and converges to $\mathrm{RMSE}$ of MACIN for lead times of $3\mathrm{min}$ and more. *Cloudmask variation* point $\mathrm{MBE}$ is in the beginning about $0\mathrm{Wm}^{-2}$, negative $\mathrm{MBE}$ of MACIN especially during the first minutes of the nowcasts can therefore be associated to erroneous cloudmasks in the vicinity of the sun. The minor improvement for larger lead times when using perfect cloudmasks might also be a result of the convectively growing, shrinking and reshaping clouds. As the nowcasting model cannot describe these processes, perfectly outlining clouds in the beginning may not be that relevant for longer lead times. Non-zero $\mathrm{RMSE}$ of the *cloudmask variation* for lead time $0\mathrm{min}$ may result from errors in the RT parametrization or smearing out by assimilation, as described for MACIN before. To further investigate implications of the RT parametrization, the *continuous cloudmask variation* was run. It differs from MACIN only by the input cloudmasks. In contrast to the *cloudmask variation*, which gives discrete cloudmask values for *clearsky* and *cloudy*, the *continuous cloudmask variation* relies on cloudmasks with continuous values. The RT parametrization maps model cloudiness states linearly to DNI values. Model cloudiness states of MACIN usually rely on CNN cloudmasks with discrete values for the three classes (*clearsky*,

*cloudy*, *undecided*) while actual cloud optical depth is a continuous variable. Continuous cloudmasks are used to check whether this discrete representation causes a significant fraction of nowcast error. These cloudmasks are derived from $\tau$ used for the cloudmask validation, but comply with the exponential attenuation of intensity in radiative transfer by $\mathrm{cm}_{\mathrm{cont}} = 1 - \exp(\tau)$. The *continuous cloudmask variation* uses these continuous cloudmasks. Resulting errors of the *continuous cloudmask variation* are not depicted as they strongly resemble errors of the *cloudmask variation* with slight improvements of $\mathrm{RMSE}$ in the range of about $5\mathrm{Wm}^{-2}$. Therefore, we conclude that the RT parametrization and discrete nature of cloudmasks is not a major error source and non-zero $\mathrm{RMSE}$ for lead time $0\mathrm{min}$ is a result of smearing out during assimilation.

A further variation of MACIN was run to assess the benefits of the assimilation scheme. Therefore, the *simple variation* of MACIN was run with just a single cloudmask and velocity field from the ASI at P1 as input. The sun region is not masked out in cloudmask and velocity field for the *simple variation*. With this variation, we assess possible benefits from the additional complexity and computational cost of MACIN. Resulting errors differ from errors of MACIN mainly for point nowcasts. For lead time $0\mathrm{min}$, $\mathrm{RMSE}$ of the *simple variation* is about $300\mathrm{Wm}^{-2}$. For larger lead times, $\mathrm{RMSE}$ resembles $\mathrm{RMSE}$ of MACIN but is approximately $75\mathrm{Wm}^{-2}$ larger. $\mathrm{MBE}$ of the *simple variation* is strongly negative with values around $75\mathrm{Wm}^{-2}$ and even more for lead time $0\mathrm{min}$. As the sun region is not masked out in the *simple variation* and the cloudmask CNN tends to classify the sun in synthetic images as *cloudy*, the initial model cloudiness state is incorrect in this region and derived DNI for lead time $0\mathrm{min}$ gives large errors. In case of clearsky the erroneously *cloudy* detected sun is steady and therefore this "cloud" does not move and gives an offset for all lead times. This explains the large $\mathrm{RMSE}$ offset and the large negative $\mathrm{MBE}$. We are aware that these larger errors are mainly due to the co-location of ASI and nowcasted point in our setup. Still, this demonstrates the capabilities of our nowcasting model to use multiple data sources for error reduction. E.g., when using projected images of ASIs at different positions and superimposing one over the other for derived CBH, the sun is in different regions of the images. When we exclude, per ASI, the immediate region of the sun from used cloudmask, cloudmask information from another ASI is used to fill in this region. Thus, erroneous cloudmasks in the region of the sun can be mitigated by assimilation.

In general, the nowcast quality is influenced by the variability of DNI. Completely cloud free and also fully overcast situations result in low variability and are simple to nowcast. Broken clouds can cause strong variations in DNI and are more challenging to nowcast. Other nowcasting systems in the literature (e.g., Nouri et al., 2019) are therefore benchmarked not just on all available situations but also separately on situations grouped into 8 variability classes. This showcases the nowcast quality under different weather conditions and variabilities. We investigated the performance of MACIN by computing error metrics for subsets of the 359 nowcasts of this study. The subsets were determined by cloud fraction. Overall, small absolute $\mathrm{RMSE}$ can be found especially for small and large cloud fractions with minor to no improvements of MACIN over persistence. Errors are larger for broken clouds and medium cloud fractions and the improvement of MACIN over persistence increases in these cases. However, the significance of these cloud fraction dependent results is limited due to the small number of nowcasts and the restriction to the shallow cumulus LES data. It is therefore not displayed and discussed here in detail.

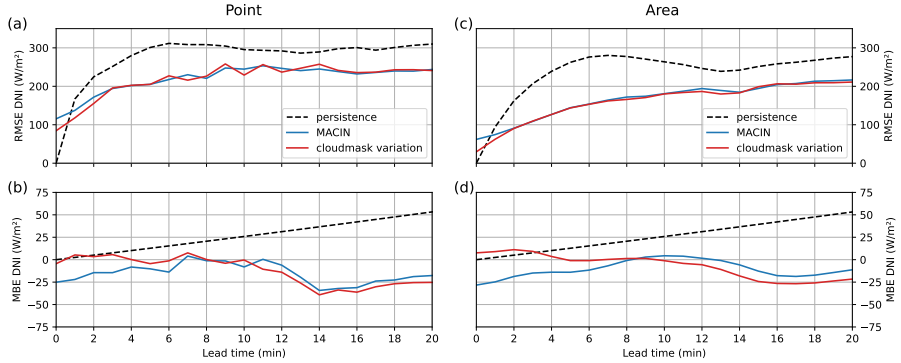


**Figure 6.** (a) RMSE and (b) MBE for 359 point DNI nowcasts compared to DNI point reference values and evaluated per lead time. Nowcasts were done using MACIN and the *cloudmask variation*. (c) and (d) show corresponding error values for area nowcasts and DNI area reference.

## 4 Conclusions

In this study, we introduced the novel all-sky imager (ASI) based direct normal irradiance (DNI) nowcasting model MACIN, which adapts ideas of 4D-Var data assimilation. We validated MACIN against synthetic data from LES cloud scenes. The nowcasting model is designed to consider setups with multiple ASI and to nowcast DNI for points and areas. We derive cloudmasks, cloud base height and cloud motion from ASI images and combine these into an initial cloudiness state for a 2-dimensional horizontal advection model. Predicted cloudiness states are projected to the ground and converted to DNI using previous DNI values.

Cloud scenes from a shallow cumulus cloud field computed using UCLA-LES (Stevens et al., 2005) with cloud fraction between 0% and 100% were used for validation and in-depth analysis of the nowcasting system and its components. For these cloud scenes, synthetic ASI images were generated. DNI at the ground was calculated for synthetic point and area reference values. References for cloud optical depth and cloud base height were derived for ASI by tracing through cloud scenes. With this data, we validated our methods for cloud detection relying on a CNN, cloud base height derivation from stereography, and cloud motion derivation from sparse feature matching of consecutive images. The synthetic setup facilitated a comparison of DNI nowcasts from MACIN against point and area references usually unavailable from observations. Thereby we could confirm previous findings of a RMSE reduction by spatial aggregation for nowcasts by Kuhn et al. (2018a). Overall, we find improvements over persistence. In general, errors correspond to findings for other ASI based nowcasting systems in literature (e.g., Peng et al., 2015; Schmidt et al., 2016; Nouri et al., 2022). MACIN gives non-zero errors for point nowcasts from the beginning, as also observed in e.g. Schmidt et al. (2016) and Peng et al. (2015). Deriving reference cloudmasks from LES cloud optical depth allowed for an attribution of initial errors of MACIN to imperfect cloudmasks in the vicinity of the sun, imperfect DNI estimation, and a smoothing of the initial state by assimilation. For applications where these initial errors are crucial, they could easily be reduced by using persistence nowcasts for small lead times and nowcasts of MACIN for larger

lead times, as suggested by Nouri et al. (2022). We did not address this further as it is unlikely to be relevant for operational use, given that an immediate computation of DNI nowcast, transfer to consumers and reaction of their system seem unrealistic. By comparing further simplified nowcasts relying only on a single imager, we demonstrate the capability of the nowcasting model to make beneficial use of multiple ASIs and the assimilation scheme.

A limitation of this study is the restricted set of $360\mathrm{min}$ of cloud data and a single constant sun zenith angle. Future work will apply the nowcasting model to real world data to consider manifold cloud scenes and sun positions. This step is necessary to further confirm the benefits of the model. Additionally, we plan to use the synthetic setup for in-depth investigation of theoretical error sources of ASI nowcasts, e.g., to investigate errors introduced by using advection to predict future cloud states and neglecting convective development of clouds.

*Data availability.* The LES cloud data used for this study is published (Jakub and Gregor, 2022) and can be obtained at https://opendata.physik.lmu.de/5d0k9-q2n86. For further data, e.g., the full syntetic image sets or reference DNIs please contact the authors of this study.

## Appendix A

### A1 Cloudmask CNN

Convolutional neural networks (CNN) are used frequently in image segmentation tasks. The wide variety of possible atmospheric conditions, ligth situations and cloud types even within single ASI images allows only for limited success with classical e.g. color and threshold based methods for cloudmask derivation. E.g. Dev et al. (2019) demonstrated the possibility to use CNNs for segmentation of all-sky images, Fabel et al. (2022) even demonstrates a segmentation into different classes of clouds.

For the application of a single layer advection model, we aim at a segmentation between cloudy and clear areas of an image. A major piece of work is the generation of training images. As the nowcasting model and CNN is intended for real world applications beyond this study, real images captured with a ASI-16 were used. This also avoids overfitting on the limited number of synthetic ASI images generated for the LES scene. 793 real ASI images were hand labeled and split into a train and validation dataset of 635 and 158 images respectively. These are normalized using the channel-wise mean and standard deviation over all training images. All images of both datasets were scaled to $512 \times 512$ pixel. For training, random excerpts of $256 \times 256$ pixel were cropped and randomly mirrored or rotated by $90°$ to artificially increase the amount of training data by augmentation. Hand labeling was done through a tool we designed for this task, which subdivided a randomly chosen and projected ASI training image into so called superpixels (Achanta et al., 2012), continuous regions with similar color information and limited distance. Each superpixel can be assigned on of the three classes *cloudy*, *clear* or *undecided*. The subdivision into superpixels allows for faster labeling of pixels belonging together. The labeling tool allows for the selection of the number of superpixels, therefore also small regions may be labeled precisely. As clouds and clearsky are not always precisely distinguishable and their definition based on visual appearance is hard, we also offered the label *undecided*. This label marks regions which are hard or cumbersome for humans to classify and therefore left out. In the training of the neural

network these *undecided* pixels are considered as such, i.e. the CNN is not challenged to label these regions according to potentially miss-labeled training data but may learn more from regions where humans are sure about the proper label. Example images from the validation set, corresponding hand labeled segmentation and CNN segmentation are shown in Fig. A1. The CNN and its training is described in the following. We chose the DeeplabV3+ (Chen et al., 2018) CNN architecture which is designed using an Encoder-Decoder structure as also the UNet (Ronneberger et al., 2015) used by Fabel et al. (2022) does. For the encoder, we use a ResNet34 (He et al., 2015) pre-trained on the Imagenet dataset (Russakovsky et al., 2014). Three output channels were chosen associated to the three classes. Training was done using the Adam optimizer (Kingma and Ba, 2014) with a custom sparse-soft-cross-entropy loss (ssce). This ssce actively ignores pixels which are labeled as *undecided* in the ground truth and only focuses on *cloudy* and *clear* pixels in the ground truth. This is done using

$$y_{\mathrm{mask},i,j} = 1 - y_{\mathrm{gt},i,j,\mathrm{undecided}} \tag{A1}$$

$$\mathrm{LogSoftmax}(y_{i,j,c}) = \log\left(\frac{\exp(y_{i,j,c})}{\sum_d \exp(y_{i,j,d})}\right) \tag{A2}$$

$$\mathrm{ssce}_{i,j} = \sum_{c\in\{\mathrm{cloudy},\mathrm{clear}\}} \mathrm{LogSoftmax}(y_{\mathrm{pr},i,j,c}) \cdot y_{\mathrm{gt},i,j,c} \cdot y_{\mathrm{mask},i,j} \tag{A3}$$

where $y_{\mathrm{pr},i,j,c}$ is the predicted value for the $i$-th pixel of the $j$-th training image and the class $c$. Correspondingly, $y_{\mathrm{gt},i,j,c} \in \{0,1\}$ is the ground truth value. While ssce is necessary for optimization, this loss is meant to give mainly intermediate scores of performance of the segmentation CNN. Therefore, also a metric called mean intersection-over-union ($mIoU$) is used in a sparse version as

$$\mathrm{I} = \sum_{i,j} \sum_{c\in\{\mathrm{cloudy},\mathrm{clear}\}} y_{\mathrm{gt},i,jc} \cdot y_{\mathrm{pr},i,j,c} \cdot y_{\mathrm{mask},i,j} \tag{A4}$$

$$\mathrm{U} = \sum_{i,j} \sum_{c\in\{\mathrm{cloudy},\mathrm{clear}\}} (y_{\mathrm{gt},i,j,c} + y_{\mathrm{pr},i,j,c}) \cdot y_{\mathrm{mask},i,j} - \mathrm{I} \tag{A5}$$

$$\mathrm{mIoU} = \frac{\mathrm{I}}{\mathrm{U}+\epsilon} \tag{A6}$$

with $\epsilon = 10^{-7}$ for numerical stability. This metric is designed to represent a ratio between correctly classified pixels in comparison to overall classified pixels, again adapted by us to ignore *undecided* ground truth pixels. It was computed after every epoch on the entire validation dataset. We used a batch size of $26$ images and a learning rate of $7 \times 10^{-5}$. After $48$ epochs of training, $\mathrm{mIoU} = 0.968$ was reached for the CNN as used within this study. For the prediction of cloudmasks, the label of a pixel is derived from the output channel with maximum value. This is mapped to scalar values as $0$ for *clear*, $1$ for *cloudy* and $0.5$ for *undecided* to obtain the final CNN cloudmasks.

*Author contributions.* PG developed the nowcasting model, performed the validation and wrote the manuscript in its current form. FJ computed the LES cloud fields and supported their integration into this study. TZ and BM assisted the model development and validation and contributed to the manuscript. TZ and BM prepared the proposal for the BMEL project.

*Competing interests.* At least one of the (co-)authors is a member of the editorial board of Atmospheric Measurement Techniques. The peer-review process was guided by an independent editor, and the authors also have no other competing interests to declare.

*Acknowledgements.* This work was supported by the German Federal Ministry of Food and Agriculture (BMEL) through the FNR (Fachagentur Nachwachsende Rohstoffe e.V.) project NETFLEX-LMU FKZ22400318. We are grateful to Josef Schreder for the support and professional advice in context of all-sky imagers, especially the CMS Schreder ASI-16 imagers. Additionally, Josef Schreder supported this work on behalf of the CMS - ING. DR. SCHREDER GMBH by providing the ASI-16 all-sky imagers. Images of ASI-16 were used in the development of the cloudmask algorithm. The synthetic ASI used throughout this studied was modelled to resemble the geometry of an ASI-16. We would also like to thank the two anonymous reviewers for their comments that improved the quality of the manuscript.

## References


Achanta, R., Shaji, A., Smith, K., Lucchi, A., Fua, P., and Süsstrunk, S.: SLIC Superpixels Compared to State-of-the-Art Superpixel Methods, IEEE Transactions on Pattern Analysis and Machine Intelligence, 34, 2274–2282, https://doi.org/10.1109/TPAMI.2012.120, 2012.

Anderson, G. P., Clough, S. A., Kneizys, F. X., Chetwynd, J. H., and Shettle, E. P.: AFGL atmospheric constituent profiles (0–120 km), Tech. Rep. 954, Air Force Geophysics Lab Hanscom AFB MA, 1986.

Beekmans, C., Schneider, J., Läbe, T., Lennefer, M., Stachniss, C., and Simmer, C.: Cloud photogrammetry with dense stereo for fisheye cameras, Atmospheric Chemistry and Physics, 16, 14 231–14 248, https://doi.org/10.5194/acp-16-14231-2016, 2016.

Blum, N. B., Nouri, B., Wilbert, S., Schmidt, T., Lünsdorf, O., Stührenberg, J., Heinemann, D., Kazantzidis, A., and Pitz-Paal, R.: Cloud height measurement by a network of all-sky imagers, Atmospheric Measurement Techniques, 14, 5199–5224, https://doi.org/10.5194/amt-14-5199-2021, 2021.

Blum, N. B., Wilbert, S., Nouri, B., Stührenberg, J., Lezaca Galeano, J. E., Schmidt, T., Heinemann, D., Vogt, T., Kazantzidis, A., and Pitz-Paal, R.: Analyzing Spatial Variations of Cloud Attenuation by a Network of All-Sky Imagers, Remote Sensing, 14, 5685, https://doi.org/10.3390/rs14225685, 2022.

Boudreault, L.-É., Liandrat, O., Braun, A., Buessler, É., Lafuma, M., Cros, S., Gomez, A., Sas, R., and Delmas, J.: Sky-Imager Forecasting for Improved Management of a Hybrid Photovoltaic-Diesel System, 3rd International Hybrid Power Systems Workshop, pp. 1–6, 2018.

Bradski, G.: The OpenCV Library, Dr. Dobb's Journal of Software Tools, 2000.

Bugliaro, L., Zinner, T., Keil, C., Mayer, B., Hollmann, R., Reuter, M., and Thomas, W.: Validation of cloud property retrievals with simulated satellite radiances: a case study for SEVIRI, Atmospheric Chemistry and Physics, 11, 5603–5624, https://doi.org/10.5194/acp-11-5603-2011, 2011.

Chen, L.-C., Zhu, Y., Papandreou, G., Schroff, F., and Adam, H.: Encoder-Decoder with Atrous Separable Convolution for Semantic Image Segmentation, Lecture Notes in Computer Science (including subseries Lecture Notes in Artificial Intelligence and Lecture Notes in Bioinformatics), 11211 LNCS, 833–851, https://doi.org/10.48550/arXiv.1802.02611, 2018.

Chen, X., Du, Y., Lim, E., Fang, L., and Yan, K.: Towards the applicability of solar nowcasting: A practice on predictive PV power ramp-rate control, Renewable Energy, 195, 147–166, https://doi.org/10.1016/j.renene.2022.05.166, 2022.

Chow, C. W., Urquhart, B., Lave, M., Dominguez, A., Kleissl, J., Shields, J., and Washom, B.: Intra-hour forecasting with a total sky imager at the UC San Diego solar energy testbed, Solar Energy, 85, 2881–2893, https://doi.org/10.1016/j.solener.2011.08.025, 2011.

Dev, S., Manandhar, S., Lee, Y. H., and Winkler, S.: Multi-label Cloud Segmentation Using a Deep Network, 2019 USNC-URSI Radio Science Meeting (Joint with AP-S Symposium), USNC-URSI 2019 - Proceedings, pp. 113–114, https://doi.org/10.1109/USNC-URSI.2019.8861850, 2019.

Fabel, Y., Nouri, B., Wilbert, S., Blum, N., Triebel, R., Hasenbalg, M., Kuhn, P., Zarzalejo, L. F., and Pitz-Paal, R.: Applying self-supervised learning for semantic cloud segmentation of all-sky images, Atmospheric Measurement Techniques, 15, 797–809, https://doi.org/10.5194/amt-15-797-2022, 2022.

Hasenbalg, M., Kuhn, P., Wilbert, S., Nouri, B., and Kazantzidis, A.: Benchmarking of six cloud segmentation algorithms for ground-based all-sky imagers, Solar Energy, 201, 596–614, https://doi.org/10.1016/j.solener.2020.02.042, 2020.

He, K., Zhang, X., Ren, S., and Sun, J.: Deep Residual Learning for Image Recognition, Proceedings of the IEEE Computer Society Conference on Computer Vision and Pattern Recognition, 2016-Decem, 770–778, https://doi.org/10.1109/CVPR.2016.90, 2015.

Hillaire, S.: Physically Based Sky, Atmosphere and Cloud Rendering in Frostbite, SIGGRAPH 2016 Course, https://www.ea.com/frostbite/news/physically-based-sky-atmosphere-and-cloud-rendering, 2016.

Hu, Y., Song, R., and Li, Y.: Efficient Coarse-to-Fine Patch Match for Large Displacement Optical Flow, in: 2016 IEEE Conference on Computer Vision and Pattern Recognition (CVPR), vol. 2016-Decem, pp. 5704–5712, IEEE, https://doi.org/10.1109/CVPR.2016.615, 2016.

Jakub, F. and Gregor, P.: UCLA-LES shallow cumulus dataset with 3D cloud output data, https://doi.org/https://doi.org/10.57970/5d0k9-q2n86, 2022.

Katiraei, F. and Agüero, J. R.: Solar PV integration challenges, IEEE Power and Energy Magazine, 9, 62–71, https://doi.org/10.1109/MPE.2011.940579, 2011.

Kazantzidis, A., Tzoumanikas, P., Blanc, P., Massip, P., Wilbert, S., and Ramirez-Santigosa, L.: Short-term forecasting based on all-sky cameras, Ccd, Elsevier Ltd, https://doi.org/10.1016/B978-0-08-100504-0.00005-6, 2017.

Kingma, D. P. and Ba, J.: Adam: A Method for Stochastic Optimization, 3rd International Conference on Learning Representations, ICLR 2015 - Conference Track Proceedings, pp. 1–15, http://arxiv.org/abs/1412.6980, 2014.

Kölling, T., Zinner, T., and Mayer, B.: Aircraft-based stereographic reconstruction of 3-D cloud geometry, Atmospheric Measurement Techniques, 12, 1155–1166, https://doi.org/10.5194/amt-12-1155-2019, 2019.

Kuhn, P., Wilbert, S., Prahl, C., Schüler, D., Haase, T., Hirsch, T., Wittmann, M., Ramirez, L., Zarzalejo, L., Meyer, A., Vuilleumier, L., Blanc, P., and Pitz-Paal, R.: Shadow camera system for the generation of solar irradiance maps, Solar Energy, 157, 157–170, https://doi.org/10.1016/j.solener.2017.05.074, 2017a.

Kuhn, P., Wilbert, S., Schüler, D., Prahl, C., Haase, T., Ramirez, L., Zarzalejo, L., Meyer, A., Vuilleumier, L., Blanc, P., Dubrana, J., Kazantzidis, A., Schroedter-Homscheidt, M., Hirsch, T., and Pitz-Paal, R.: Validation of spatially resolved all sky imager derived DNI nowcasts, in: AIP Conference Proceedings, vol. 1850, p. 140014, https://doi.org/10.1063/1.4984522, 2017b.

Kuhn, P., Nouri, B., Wilbert, S., Prahl, C., Kozonek, N., Schmidt, T., Yasser, Z., Ramirez, L., Zarzalejo, L., Meyer, A., Vuilleumier, L., Heinemann, D., Blanc, P., and Pitz-Paal, R.: Validation of an all-sky imager–based nowcasting system for industrial PV plants, Progress in Photovoltaics: Research and Applications, 26, 608–621, https://doi.org/10.1002/pip.2968, 2018a.

Kuhn, P., Wirtz, M., Killius, N., Wilbert, S., Bosch, J., Hanrieder, N., Nouri, B., Kleissl, J., Ramirez, L., Schroedter-Homscheidt, M., Heinemann, D., Kazantzidis, A., Blanc, P., and Pitz-Paal, R.: Benchmarking three low-cost, low-maintenance cloud height measurement systems and ECMWF cloud heights against a ceilometer, Solar Energy, 168, 140–152, https://doi.org/10.1016/j.solener.2018.02.050, 2018b.

Kuhn, P., Nouri, B., Wilbert, S., Hanrieder, N., Prahl, C., Ramirez, L., Zarzalejo, L., Schmidt, T., Yasser, Z., Heinemann, D., Tzoumanikas, P., Kazantzidis, A., Kleissl, J., Blanc, P., and Pitz-Paal, R.: Determination of the optimal camera distance for cloud height measurements with two all-sky imagers, Solar Energy, 179, 74–88, https://doi.org/10.1016/j.solener.2018.12.038, 2019.

Kurtz, B., Mejia, F., and Kleissl, J.: A virtual sky imager testbed for solar energy forecasting, Solar Energy, 158, 753–759, https://doi.org/10.1016/j.solener.2017.10.036, 2017.

Kylling, A., Stamnes, K., and Tsay, S. C.: A reliable and efficient two-stream algorithm for spherical radiative transfer: Documentation of accuracy in realistic layered media, Journal of Atmospheric Chemistry, 21, 115–150, https://doi.org/10.1007/BF00696577, 1995.

Law, E. W., Kay, M., and Taylor, R. A.: Evaluating the benefits of using short-term direct normal irradiance forecasts to operate a concentrated solar thermal plant, Solar Energy, 140, 93–108, https://doi.org/10.1016/j.solener.2016.10.037, 2016.

Le Dimet, F.-X. and Talagrand, O.: Variational algorithms for analysis and assimilation of meteorological observations: theoretical aspects, Tellus A: Dynamic Meteorology and Oceanography, 38, 97–110, https://doi.org/10.3402/tellusa.v38i2.11706, 1986.

Li, Q., Lu, W., and Yang, J.: A hybrid thresholding algorithm for cloud detection on ground-based color images, Journal of Atmospheric and Oceanic Technology, 28, 1286–1296, https://doi.org/10.1175/JTECH-D-11-00009.1, 2011.

Masuda, R., Iwabuchi, H., Schmidt, K. S., Damiani, A., and Kudo, R.: Retrieval of Cloud Optical Thickness from Sky-View Camera Images using a Deep Convolutional Neural Network based on Three-Dimensional Radiative Transfer, Remote Sensing, 11, 1962, https://doi.org/10.3390/rs11171962, 2019.

Mayer, B.: Radiative transfer in the cloudy atmosphere, The European Physical Journal Conferences, 1, 75–99, https://doi.org/10.1140/epjconf/e2009-00912-1, 2009.

Nguyen, D. A. and Kleissl, J.: Stereographic methods for cloud base height determination using two sky imagers, Solar Energy, 107, 495–509, https://doi.org/10.1016/j.solener.2014.05.005, 2014.

Nouri, B., Kuhn, P., Wilbert, S., Prahl, C., Pitz-Paal, R., Blanc, P., Schmidt, T., Yasser, Z., Santigosa, L. R., and Heineman, D.: Nowcasting of DNI maps for the solar field based on voxel carving and individual 3D cloud objects from all sky images, AIP Conference Proceedings, 2033, https://doi.org/10.1063/1.5067196, 2018.

Nouri, B., Wilbert, S., Kuhn, P., Hanrieder, N., Schroedter-Homscheidt, M., Kazantzidis, A., Zarzalejo, L., Blanc, P., Kumar, S., Goswami, N., Shankar, R., Affolter, R., and Pitz-Paal, R.: Real-time uncertainty specification of all sky imager derived irradiance nowcasts, Remote Sensing, 11, https://doi.org/10.3390/rs11091059, 2019.

Nouri, B., Blum, N., Wilbert, S., and Zarzalejo, L. F.: A Hybrid Solar Irradiance Nowcasting Approach: Combining All Sky Imager Systems and Persistence Irradiance Models for Increased Accuracy, Solar RRL, 6, 1–12, https://doi.org/10.1002/solr.202100442, 2022.

Paszke, A., Gross, S., Massa, F., Lerer, A., Bradbury, J., Chanan, G., Killeen, T., Lin, Z., Gimelshein, N., Antiga, L., Desmaison, A., Kopf, A., Yang, E., DeVito, Z., Raison, M., Tejani, A., Chilamkurthy, S., Steiner, B., Fang, L., Bai, J., and Chintala, S.: PyTorch: An Imperative Style, High-Performance Deep Learning Library, in: Advances in Neural Information Processing Systems 32, edited by Wallach, H., Larochelle, H., Beygelzimer, A., d\textquotesingle Alché-Buc, F., Fox, E., and Garnett, R., pp. 8024–8035, Curran Associates, Inc., http://papers.neurips.cc/paper/9015-pytorch-an-imperative-style-high-performance-deep-learning-library.pdf, 2019.

Peng, Z., Yu, D., Huang, D., Heiser, J., Yoo, S., and Kalb, P.: 3D cloud detection and tracking system for solar forecast using multiple sky imagers, Solar Energy, 118, 496–519, https://doi.org/10.1016/j.solener.2015.05.037, 2015.

Rodríguez-Benítez, F. J., López-Cuesta, M., Arbizu-Barrena, C., Fernández-León, M. M., Pamos-Ureña, M. Á., Tovar-Pescador, J., Santos-Alamillos, F. J., and Pozo-Vázquez, D.: Assessment of new solar radiation nowcasting methods based on sky-camera and satellite imagery, Applied Energy, 292, 116 838, https://doi.org/10.1016/j.apenergy.2021.116838, 2021.

Ronneberger, O., Fischer, P., and Brox, T.: U-Net: Convolutional Networks for Biomedical Image Segmentation, IEEE Access, 9, 16 591–16 603, https://doi.org/10.1109/ACCESS.2021.3053408, 2015.

Russakovsky, O., Deng, J., Su, H., Krause, J., Satheesh, S., Ma, S., Huang, Z., Karpathy, A., Khosla, A., Bernstein, M., Berg, A. C., and Fei-Fei, L.: ImageNet Large Scale Visual Recognition Challenge, http://arxiv.org/abs/1409.0575, 2014.

Saleh, M., Meek, L., Masoum, M. A., and Abshar, M.: Battery-less short-term smoothing of photovoltaic generation using sky camera, IEEE Transactions on Industrial Informatics, 14, 403–414, https://doi.org/10.1109/TII.2017.2767038, 2018.

Samu, R., Calais, M., Shafiullah, G. M., Moghbel, M., Shoeb, M. A., Nouri, B., and Blum, N.: Applications for solar irradiance nowcasting in the control of microgrids: A review, Renewable and Sustainable Energy Reviews, 147, 111 187, https://doi.org/10.1016/j.rser.2021.111187, 2021.

Schmidt, T., Kalisch, J., Lorenz, E., and Heinemann, D.: Evaluating the spatiooral performance of sky-imager-based solar irradiance analysis and forecasts, Atmospheric Chemistry and Physics, 16, 3399–3412, https://doi.org/10.5194/acp-16-3399-2016, 2016.

Schneider, A.: Real-time volumetric cloudscapes, in: GPU Pro 360 Guide to Lighting, pp. 473–504, AK Peters/CRC Press, 2018.

Shields, J., Karr, M., Burden, A., Johnson, R., Mikuls, V., Streeter, J., and Hodgkiss, W.: Research toward Multi-site Characterization of Sky Obscuration by Clouds, Final Report for GrantN00244-07-1-009, Tech. rep., Marine Physical Laboratory, Scripps Institution of Oceanography, University of California,, San Diego, USA, 2009.

Stevens, B., Moeng, C.-H., Ackerman, A. S., Bretherton, C. S., Chlond, A., de Roode, S., Edwards, J., Golaz, J.-C., Jiang, H., Khairoutdinov, M., Kirkpatrick, M. P., Lewellen, D. C., Lock, A., Müller, F., Stevens, D. E., Whelan, E., and Zhu, P.: Evaluation of Large-Eddy Simulations via Observations of Nocturnal Marine Stratocumulus, Monthly Weather Review, 133, 1443–1462, https://doi.org/10.1175/MWR2930.1, 2005.

Tola, E., Lepetit, V., and Fua, P.: DAISY: An Efficient Dense Descriptor Applied to Wide-Baseline Stereo, IEEE Transactions on Pattern Analysis and Machine Intelligence, 32, 815–830, https://doi.org/10.1109/TPAMI.2009.77, 2010.

West, S. R., Rowe, D., Sayeef, S., and Berry, A.: Short-term irradiance forecasting using skycams: Motivation and development, Solar Energy, 110, 188–207, https://doi.org/10.1016/j.solener.2014.08.038, 2014.

Xie, W., Liu, D., Yang, M., Chen, S., Wang, B., Wang, Z., Xia, Y., Liu, Y., Wang, Y., and Zhang, C.: SegCloud: A novel cloud image segmentation model using a deep convolutional neural network for ground-based all-sky-view camera observation, Atmospheric Measurement Techniques, 13, 1953–1961, https://doi.org/10.5194/amt-13-1953-2020, 2020.

Ye, L., Cao, Z., and Xiao, Y.: DeepCloud: Ground-Based Cloud Image Categorization Using Deep Convolutional Features, IEEE Transactions on Geoscience and Remote Sensing, 55, 5729–5740, https://doi.org/10.1109/TGRS.2017.2712809, 2017.

Zhu, C., Byrd, R. H., Lu, P., and Nocedal, J.: Algorithm 778: L-BFGS-B, ACM Transactions on Mathematical Software, 23, 550–560, https://doi.org/10.1145/279232.279236, 1997.

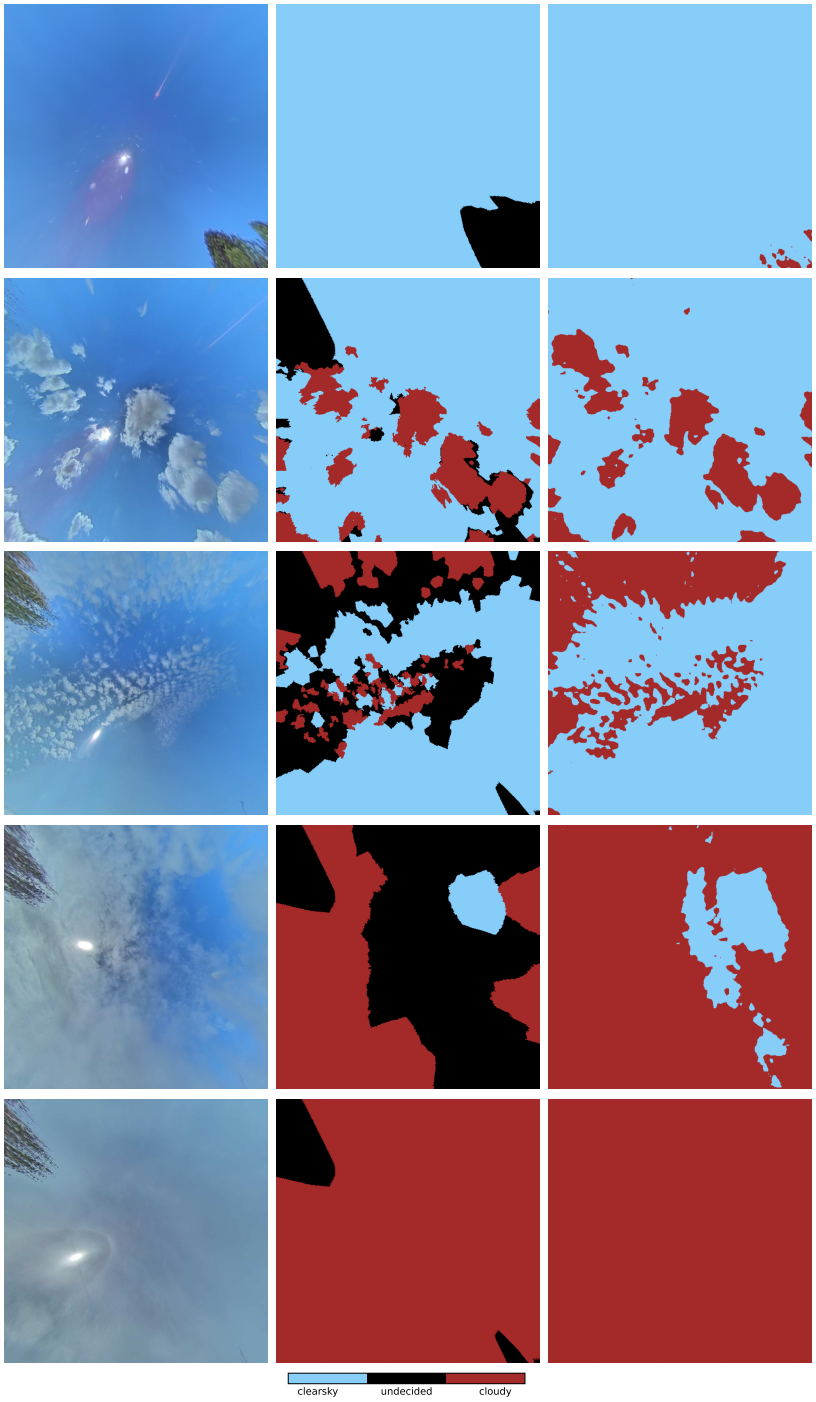


**Figure A1.** Example images from the validation set (left) hand labeled segmentation (middle) and cloudmask predicted by the trained CNN (right).